

Micro-SQUID characteristics

K. Hasselbach

CRTBT-CNRS, 25 avenue des Martyrs, BP 166 X, 38042 Grenoble, France

D. Mailly

LPN-CNRS, 196 H. Ravera, 92220 Bagneux, France

J.R. Kirtley

IBM T.J. Watson Research Center, Yorktown Heights, NY 10598, USA

(November 11, 2018)

We report on the dependence on field and temperature of the critical current of micro-SQUIDs: SQUIDs with diameters as small as 1 micron, using Dayem bridges as weak links. We model these SQUIDs by solving the Ginzburg-Landau equations with appropriate boundary conditions to obtain the supercurrent-phase relationships. These solutions show that the phase drops and depression of the order parameter produced by supercurrent flow are often distributed throughout the micro-SQUID structure, rather than being localized in the bridge area, for typical micro-SQUID geometries and coherence lengths. The resultant highly non-sinusoidal current-phase relationships $I_c(\varphi)$ lead to reduced modulation depths and triangular dependences of the micro-SQUID critical currents on applied magnetic flux $I_c(\Phi)$. Our modelling agrees well with our measurements on both Al and Nb micro-SQUIDs.

INTRODUCTION

Several different types of specialized Superconducting Quantum Interference Devices (SQUIDs) have been developed for measuring the magnetic response of small samples. One such device is the “micro-SQUID”: a thin film DC-SQUID with Dayem-Bridges as Josephson Junctions [1]. In the micro-SQUID, the entire device is fabricated by electron beam lithography, and the SQUID loop itself serves as the flux-input coil. Micro-SQUIDs have the advantages of very small pickup areas (about $1\mu\text{m}^2$), and relatively small sensitivity to in-plane applied magnetic fields (since they can be made very thin, less than 20 nm). Micro-SQUIDs have been used for the observation of persistent currents in 2 dimensional electron gas rings [2], for the study of the mechanisms of magnetization reversal in ferromagnetic particles as small as 3 nm in diameter [3,4], and have been integrated into a scanning SQUID-AFM with high magnetic field spatial resolution [5,6]. However, these SQUIDs have two disadvantages: they have hysteretic current-voltage characteristics, and relatively low modulation depths in their critical current - flux characteristics. In this paper we report detailed measurements of micro-SQUID characteristics, and compare them with model calculations. These calculations model the micro-SQUID characteristics well, and could represent a valuable tool for optimizing the properties of this class of SQUIDs.

MEASUREMENT

The basic operating properties of micro-SQUIDs are understood: They have a hysteretic $V(I)$ characteristic, induced by the propagation of a hot spot. As the current is ramped up from zero, the micro-SQUID transits from the superconducting to the normal state at a critical current I_c . A voltage step is generated as the normal state resistance of the junction appears and the dissipated energy heats the entire micro-SQUID loop. When the current is lowered the micro-SQUID stays in the resistive state until the current is much smaller than I_c . This thermal hysteresis excludes the usual current biasing schemes used for DC-SQUID readout. Therefore a detection technique suitable for hysteretic devices [7] is implemented: A computer controlled circuit simultaneously triggers a current ramp and a 40MHz quartz clock. As soon as a $\partial V/\partial t$ pulse of a preset height is detected at the micro-SQUID, the clock stops and the current is set to zero. The clock reading is transferred to the computer, and the cycle begins again. The critical current is proportional to the duration of the current ramp. The fastest repetition rate is 10kHz, limited by the time needed to settle the current. A single wire is sufficient to connect the micro-SQUID, since the $\partial V/\partial t$ pulse is detected on the current biasing lead. Every time the critical current is measured, the flux state in the micro-SQUID is sampled, and every time the micro-SQUID becomes normally conducting the external field penetrates. As the current is reduced (in 40ns) to zero the micro-SQUID structure becomes progressively superconducting again and screening currents are set up to quantize the total flux through the micro-

SQUID. In the limit of high critical currents different flux configurations can be stabilized in the micro-SQUID ring during the backswitching, leading to multivalued I_c vs B characteristics.

However, the details of the dependence of the critical current of the micro-SQUID on magnetic field and temperature have not been well characterized. We present in this manuscript a detailed description of the underlying physics necessary for the understanding and improvement of this type of SQUID. In this study we made $I_c(T)$ and I_c vs B measurements on micro-SQUID devices made of aluminum or niobium. Each SQUID consists of a $1\mu\text{m}$ square loop. Bulk aluminum and niobium have very different superconducting properties, such as the coherence length ξ , and the normal to superconducting transition temperature T_c . The characteristics of micro-SQUIDS (see e.g. Fig.'s 2 and 4) do not resemble those of ideal Josephson SQUIDS, in that they have relatively shallow modulation depths and triangular I_c vs B interference patterns at low temperatures.

We believe that these non-ideal characteristics occur because the weak links in these SQUIDS are Dayem-Bridges, with dimensions comparable to the coherence length. It is well known that “long” Josephson weak links can have non-sinusoidal Josephson current-phase relationships [8–10], and that non-sinusoidal Josephson current-phase relationships can in turn lead to non-ideal SQUID I_c vs B interference patterns [11]. Faucher et al. [12] have attributed the non-ideal critical current vs. flux characteristics of their micro-SQUIDS to the large kinetic inductance of the micro-bridges. We believe the treatment given here is equivalent to that of Faucher et al. in terms of the properties of the micro-bridges, but it goes further, in that it includes the properties of the entire SQUID loop itself. We model the SQUID current-phase relationships by solving the 2-d Ginzburg-Landau equations. It is important to solve these equations in the full geometry of the micro-SQUID, since as previously pointed out in general for Dayem-Bridges [9], and as is born out by our modelling in this particular case, the phase drops and order-parameter depression associated with supercurrent flow often extend far from the micro-bridge.

MODEL

The first Ginzburg-Landau (GL) differential equation is [13]

$$\alpha\psi + \beta |\psi|^2 \psi + \frac{1}{2m^*} \left(\frac{\hbar}{i} \vec{\nabla} - \frac{e^* \vec{A}}{c} \right)^2 \psi = 0 \quad (1)$$

where $m^* = 2m$ and $e^* = 2e$ are the mass and charge of the Cooper pair, ψ is the complex order parameter de-

scribing the superconducting state, and \vec{A} is the vector potential. The supercurrent \vec{J} is given by:

$$\vec{J} = \frac{e^* \hbar}{2m^* i} (\psi^* \vec{\nabla} \psi - \psi \vec{\nabla} \psi^*) - \frac{e^{*2}}{m^* c} \psi^* \psi \vec{A}. \quad (2)$$

For the purposes of the paper, we include the effects of the vector potential \vec{A} in a lumped circuit element model (see Eq. 12). Therefore in our solution of the GL equations we set $\vec{A} = 0$. Writing the complex order parameter as $\psi = |\psi| e^{i\varphi}$, using a coordinate system in which the SQUID is in the xy plane, and neglecting the z dependence of the gradients of ψ , the real (Eq. 3) and imaginary (Eq. 4) parts of Eq. 1 become:

$$\alpha |\psi| + \beta |\psi|^3 - \frac{\hbar^2}{2m^*} \left[\frac{d^2 |\psi|}{dx^2} - |\psi| \left(\frac{d\varphi}{dx} \right)^2 \right] - \frac{\hbar^2}{2m^*} \left[\frac{d^2 |\psi|}{dy^2} - |\psi| \left(\frac{d\varphi}{dy} \right)^2 \right] = 0 \quad (3)$$

and

$$2 \frac{d\varphi}{dx} \frac{d|\psi|}{dx} + |\psi| \frac{d^2 \varphi}{dx^2} + 2 \frac{d\varphi}{dy} \frac{d|\psi|}{dy} + |\psi| \frac{d^2 \varphi}{dy^2} = 0. \quad (4)$$

Setting $|\psi| = f |\psi|_\infty$, where f is a real function of x and y , and $|\psi|_\infty$ is the unperturbed value of the order parameter, $\beta |\psi|_\infty^2 = -\alpha = \hbar^2 / 2m^* \xi^2(T)$ [13], and using reduced units $x' = x/\xi(T)$, $y' = y/\xi(T)$, Eq. 3 becomes

$$\frac{d^2 f}{dx'^2} - f \frac{d^2 \varphi}{dx'^2} + \frac{d^2 f}{dy'^2} - f \frac{d^2 \varphi}{dy'^2} + f - f^3 = 0 \quad (5)$$

Eq. 4 becomes

$$2 \frac{df}{dx'} \frac{d\varphi}{dx'} + f \frac{d^2 \varphi}{dx'^2} + 2 \frac{df}{dy'} \frac{d\varphi}{dy'} + f \frac{d^2 \varphi}{dy'^2} = 0. \quad (6)$$

The supercurrent density \vec{J} becomes

$$\vec{J} = \frac{e^* \hbar}{m^* \xi(T)} |\psi|_\infty^2 f^2 \left[\hat{x} \frac{d\varphi}{dx'} + \hat{y} \frac{d\varphi}{dy'} \right]. \quad (7)$$

It can be shown that Eq. 6 is equivalent to setting the divergence of the supercurrent (Eq. 7) equal to zero.

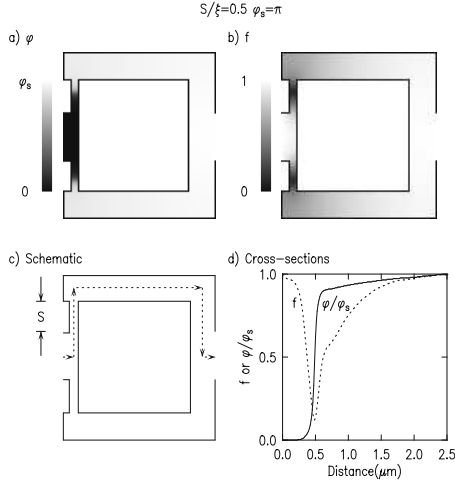


FIG. 1. Solution to the 2-dimensional Ginzburg-Landau differential equations for the quantum mechanical phase φ and normalized superfluid density f for a micro-SQUID. The geometry of the SQUID is that of the Al micro-SQUID for which measurements are presented in Fig. 4. The length of the bridge $S = 290\text{nm}$, bridge width $= 66\text{ nm}$, the SQUID length (horizontal, x) is $1.3\mu\text{m}$ and width (vertical, y) is $1.45\mu\text{m}$. The calculations for this figure were done for $\xi = 580\text{nm}$, with a total phase drop across the SQUID of $\varphi_s = \pi$. Greyscale images of the superconducting phase φ (a) and superfluid density f (b) in the SQUID are shown. Shown in (d) are cross-sections through these images, along the path shown in (c). For this value of $S/\xi(T) = 0.5$, the phase drop and superfluid depression are mostly localized in the micro-bridge region.

By taking discrete steps δ in both the x and y directions, the differential equation Eq. 5 can be cast as a difference equation

$$f_{i+1,j} + f_{i-1,j} + f_{i,j+1} + f_{i,j-1} + (-4 - (\varphi_{i+1,j} - \varphi_{i,j})^2 - (\varphi_{i,j+1} - \varphi_{i,j})^2 + \delta^2) f_{i,j} = \delta^2 f_{i,j}^3, \quad (8)$$

where i and j are indices labelling the 2-d matrices in the x and y directions respectively. Similarly, Eq. 6 becomes

$$\begin{aligned} & \varphi_{i+1,j} [f_{ij} + 2(f_{i+1,j} - f_{i,j})] + \varphi_{i-1,j} f_{i,j} \\ & + \varphi_{i,j+1} [f_{i,j} + 2(f_{i,j+1} - f_{i,j})] + \varphi_{i,j-1} f_{i,j} \\ & + \varphi_{i,j} [-4f_{i,j} - 2(f_{i+1,j} - f_{i,j}) - 2(f_{i,j+1} - f_{i,j})] = 0. \end{aligned} \quad (9)$$

Using (in MKS units) $|\psi|_\infty^2 = m/2\mu_0 e^2 \lambda_{eff}^2$, where λ_{eff} is the effective thin film penetration depth [13], the total current through the SQUID can be written as:

$$I = I_0 \sum_j f_{i,j}^2 (\varphi_{i+1,j} - \varphi_{i,j}), \quad (10)$$

where $I_0 = d\hbar/2\mu_0 e \lambda_{eff}^2$, and d is the thickness of the film from which the micro-SQUID is patterned. Supercurrent conservation requires that the sum over j in Eq. 10 be independent of the value of i chosen. This was used as a self-consistency check of the solutions presented below. The difference equations Eq. 8,9 are in the standard form

$$a_{j,l} u_{j+1,l} + b_{j,l} u_{j-1,l} + c_{j,l} u_{j,l+1} + d_{j,l} u_{j,l-1} + e_{j,l} u_{j,l} = g_{j,l}. \quad (11)$$

We solved Eq.'s 8 and 9 using a general non-linear differential equation solver subroutine (SOR) using the successive over-relaxation method with Chebyshev acceleration [14]. An initial guess was made for the matrices $f_{i,j}$ and $\varphi_{i,j}$, SOR was used to search for a solution for $f_{i,j}$ of Eq. 8 for a pre-determined number of iterations, with $\varphi_{i,j}$ fixed. The result for $f_{i,j}$ was then fixed, and a solution for $\varphi_{i,j}$ in Eq. 9 was sought for the same number of iterations. This procedure was iterated until the sum of the absolute values of the deviations from equality in Eq.'s 8 and 9 were both less than a fixed error sum value. For the results reported here, the error sum value was chosen to be 10^{-3} . This procedure gave results in agreement with those reported by Likharev and Yakobson for long 1-D microbridges [8]. For modelling of our micro-SQUIDs we chose the boundary conditions: 1) φ was fixed at 0 along the entrance to the micro-SQUID structure (at the left of Fig. 1a)), and fixed at φ_s at the exit of the micro-SQUID structure (to the right); 2) f was chosen to be 1 at both the entrance and exits to the micro-SQUID; and 3) the components of the gradients of f and φ were taken to be zero normal to the other boundaries (solid lines in Fig. 1a,b). The boundaries of the model calculations were chosen to match those of electron micrographs of the actual SQUIDs measured. In choosing these boundary conditions we neglect the effects of phase drops and supercurrent depression in the leads to and from the micro-SQUID. We argue that phase drops outside of the SQUID loop should have little effect on the critical current-flux characteristics which we are modelling, and that neglect of lead effects is therefore a good starting approximation.

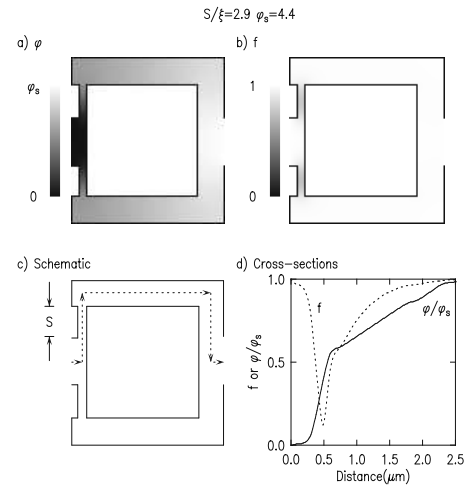


FIG. 2. Calculations for the same geometry as Fig. 1, but in this case for $S/\xi = 2.9$, with a total phase drop $\varphi_s = 4.4$. In this case both the phase drop and superfluid density depression extend throughout the SQUID structure.

Example solutions for φ and f using this model are shown in Fig.'s 1 and 2. Here the geometry is that of the Al micro-SQUID. The $\varphi_{i,j}$ and $f_{i,j}$ matrices both had 102×110 elements, with 76 elements/ μm . The bridges were $S=289$ nm long and 66 nm wide. The arms of the SQUID were 237 nm wide. Figure 1 shows the solution to Eq.'s 8 and 9 for $S/\xi=0.5$, $\varphi_s = \pi$. For a "short" 1-d micro-bridge ($S/\xi \ll 1$) with $\varphi_s = \pi$, the solution for φ has a step from 0 to π , and a depression in f to 0, with a characteristic width of ξ , centered at the center of the bridge [15]. The numerical solution for the full SQUID structure has a step in φ and a depression in f near the center of the bridges, but there are significant changes well into the body of the SQUID, and f does not go completely to 0, meaning that I_s does not go to zero, until φ_s is slightly above π . These effects become more pronounced as S/ξ increases. Figure 2 shows the results for $S/\xi=2.9$, $\varphi_s=4.4$. This is the maximum value of φ_s for which a numerical solution to the Ginzburg-Landau equations could be found for $S/\xi=2.9$. In this case almost half of the total phase drop occurs outside of the micro-bridge region.

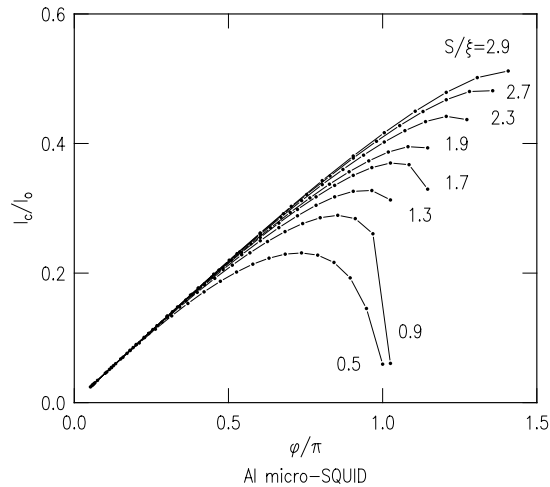


FIG. 3. Calculated supercurrent-phase relationship for the Al SQUID, for values of S/ξ appropriate for the data shown in Fig. 4

Supercurrent-phase relationships $I_s(\varphi)$ for this geometry are shown in Figure 3. This procedure is unable to find solutions numerically for the lower branch of the $I_s(\varphi)$ characteristic when this characteristic is doubly valued [8,9]. This will not affect our results, since we are comparing our modelling with the maximum supercurrent at each value of applied field. This conclusion is supported by our calculations of $I_c(\Phi)$ characteristics using the Likharev-Yakobson [8] $I_c(\varphi)$ characteristics: only the upper branch is important for calculating the $I_c(\Phi)$ characteristics. The coherence lengths ξ in Fig. 3 were chosen to be appropriate for an Al micro-SQUID at the temper-

atures for which the measurements of Fig. 4 were made: We use the dirty limit expression for the temperature dependent coherence length $\xi(T) = 0.855\sqrt{\xi_0 l / (1 - T/T_c)}$ [13], estimate the low temperature mean free path l in our films to be about 10nm from transport measurements, and take a value for ξ_0 of 100nm [16], and $T_c=1.25\text{K}$.

A SQUID with non-sinusoidal current-phase ($I_c(\varphi)$) relationships will have critical current vs. flux interference patterns ($I_c(\Phi)$) that are also non-standard. These can be modelled as follows. Assume that the SQUID has two arms labelled a and b , with total phase drops across the two arms φ_a and φ_b , inductances L_a and L_b , and micro-bridge supercurrents $I_{sa} = I_a g(\varphi_a)$ and $I_{sb} = I_b g(\varphi_b)$.

The requirement of a single valued superconducting order parameter leads to

$$2\pi n = \varphi_a - \varphi_b + 2\pi\phi_e + \beta_a g(\varphi_a) - \beta_b g(\varphi_b), \quad (12)$$

where ϕ_e is the externally applied flux Φ_e divided by the superconducting flux quantum $\Phi_0 = h/2e$, $\beta_a = 2\pi L_a I_a / \Phi_0$ and $\beta_b = 2\pi L_b I_b / \Phi_0$. The total supercurrent through the SQUID is

$$I = I_a g(\varphi_a) + I_b g(\varphi_b). \quad (13)$$

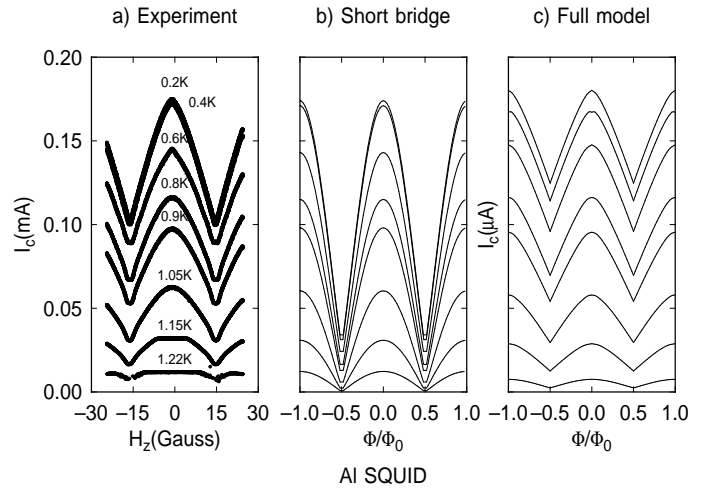


FIG. 4. (a) Experimental measurements of the critical current of an Al micro-SQUID as a function of applied field, for selected temperatures. (b) Modelling in the short-bridge limit $I=I_1 \sin\varphi$, and (c) Modelling using the full Ginzburg-Landau calculations described in the text.

The dependence of the critical current on applied field is determined most easily by assuming values for ϕ_e and one of the micro-bridge phase differences φ_a or φ_b , then varying the phase of the second micro-bridge until Eq. 12 is satisfied. The values for φ_a and φ_b are then substituted into Eq. 13 to find the total current. The maximum value for I after repeating this procedure for all initial values of φ_a and φ_b is the critical current for that value of ϕ_e . The effect of the self-induced field [7] is expressed in Eq.

12 via $\beta(T) = 2\pi LI_c(T)/\Phi_0$. $\beta(T)$ increases from T_c in proportion to the critical current, since the inductance is purely geometric. In the case of the Al micro-SQUIDS, with a critical current of $170 \mu\text{A}$ $\beta(0.2 \text{ K})$ is 0.78; in the case of Nb, which have critical currents of $2000 \mu\text{A}$, $\beta(0.2 \text{ K})$ can be as high as 8.5. However, the differences in I_c are not enough to explain the differences in the $I_c(\Phi)$ characteristics between Al and Nb: they also arise from the shorter coherence length in Nb, which leads to more highly non-sinusoidal current-phase relationships in micro-SQUIDS made from Nb.

Figure 4a shows critical current vs. applied magnetic field characteristics for our Al micro-SQUID. Figure 4b shows the prediction of Eq. 12 and Eq. 13 assuming the standard Josephson current-phase relationship $I_c = I_1 \sin(\varphi)$ for the micro-bridges. In this modelling the critical currents of the bridges and the inductances of the arms of the SQUIDS were assumed to be symmetric and the critical currents were chosen to match the zero field critical current of the SQUID at each temperature. The inductances L_a and L_b were chosen to be 0.76 pH each, half of the calculated total inductance $L = 5\mu_0 C/16$, where C is the inner circumference of the SQUID [17].

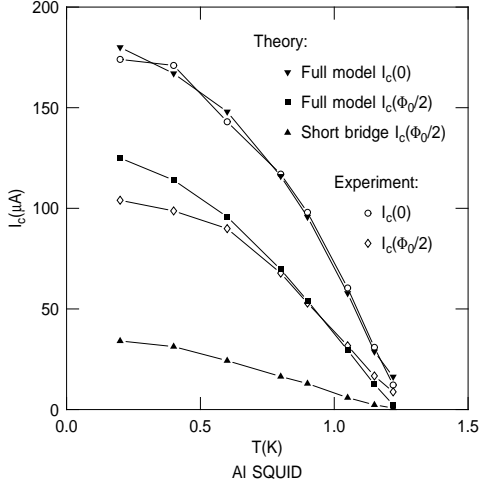


FIG. 5. Plot of the experimentally measured critical currents at zero field (open circles) and at an applied flux of half the full modulation period (open diamonds), for an Al micro-SQUID, as a function of temperature. The solid triangles are modelling as described in the text for the conventional sinusoidal current-phase relationship. The solid inverted triangles and squares are modelling using the Ginzburg-Landau calculations described in the text.

Figure 4c shows the predictions using the full GL calculations for the current-phase relationship, with the same values for the inductances. For this modelling we take $I_{ca}(\varphi_a) = I_{cb}(\varphi_b) = I_c(\varphi)/2$, where $I_c(\varphi)/I_0$ is shown for the Al micro-SQUID in Fig. 3. In the determination of I_0 we assume $\lambda_{eff}^2(T) = \lambda_{eff}^2(0)/(1 - t^4)$, $t = T/T_c$, $d = 38 \text{ nm}$ and use $\lambda_{eff}(0)$ as the sole fitting parameter. The best fit between experiment and modelling for $I_c(T, \Phi = 0)$

is for $\lambda_{eff}(0) = 172 \text{ nm}$. This is to be compared with $\lambda_L = 44 \text{ nm}$ for bulk aluminum [16]. The effective penetration depth is often longer in thin films than in bulk, and can also be increased by impurity scattering [13,16]. Further, the effective thickness of the films will be reduced by oxidation. Once this scaling is done, the agreement between theory and experiment for $I_c(T, \Phi = 0)$ is good. The full model (Figure 4c) fits the $I_c(T, \Phi)$ experimental data well. This is made clear in the plot of $I_c(0)$, the critical current at zero applied field, and $I_c(\Phi_0/2)$, the critical current at the first minimum of the interference pattern, as a function of temperature, in Figure 5. In this figure, the open circles are $I_c(0)$, and the open diamonds are $I_c(\Phi_0/2)$. The solid triangles are the predictions for a sinusoidal current-phase relationship model as outlined above. The solid squares and inverted triangles are the predictions using the GL current-phase relationship described above.

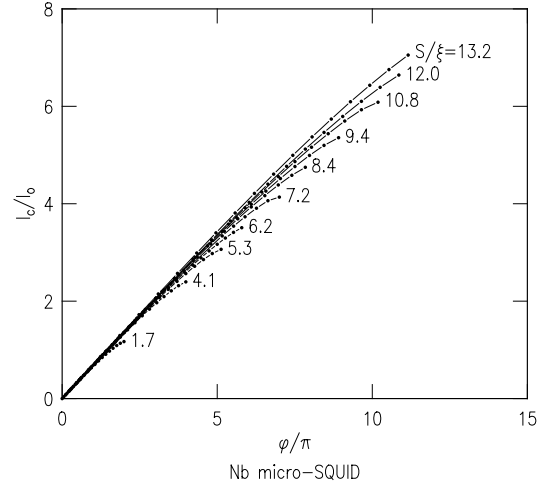


FIG. 6. Calculated supercurrent-phase relationship for the Nb SQUID, for various values of S/ξ appropriate for the data at selected temperatures shown in Fig. 7

Similar conclusions can be drawn from the data and modelling for a Nb micro-SQUID (Fig. 7). In this case the $f_{i,j}$ and $\varphi_{i,j}$ matrices were 100×100 , with 67 elements/micron. The micro-bridges were 184 nm long and 100 nm wide, with the arms of the SQUID 285 nm wide. $I_c(\varphi)$ characteristics for the values of $S/\xi(T)$ appropriate for the data of Fig. 7 are shown in Fig. 6. In this case $S/\xi(T)$ is large, the variations of φ and f are spread throughout the SQUID structure, and $I_c(\varphi)$ is nearly linear, at all temperatures. For the calculations of the $I_c(\Phi)$ characteristics in Fig. 7c, the total inductance of the SQUID was taken to be 1.4 pH , the dirty limit expression $\xi(T) = 0.855(\xi_0 l)^{1/2}/(1 - t)^{1/2}$ was again used for the coherence length, with $l = 6.5 \text{ nm}$ [10], $\xi_0 = 39 \text{ nm}$ [10], $\lambda_{eff}^2(T) = \lambda_{eff}^2(0)/(1 - t^4)$, $d = 30 \text{ nm}$, and $T_c = 8.23 \text{ K}$. Figure 7a shows experimental measurements of the depen-

dence of the SQUID critical current on applied magnetic field at selected temperatures. A multivalued critical current appears for currents higher than 0.4 and 0.5 mA for our given inductance. The sections of the $I_c(\Phi)$ characteristics are nearly linear, with sharp discontinuities in the slopes at $\Phi = (n + 1/2)\Phi_0$, n an integer.

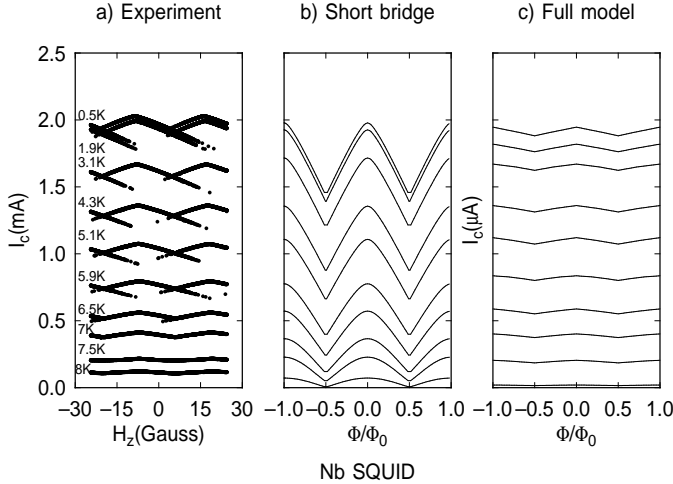


FIG. 7. (a) Experimental measurements of the critical current of an Nb micro-SQUID as a function of applied field, for selected temperatures. (b) Modelling in the short-bridge limit $I = I_1 \sin \varphi$, and (c) Modelling using the full Ginzburg-Landau calculations described in the text.

Figure 7b shows modelling for an assumed sinusoidal current-phase relationship, using symmetric experimentally determined values for the micro-bridge critical currents and symmetric inductances of 0.7pH for each arm of the SQUID. As for the Al micro-SQUID case, this modelling does poorly in describing the $I_c(\Phi)$ characteristics. Figure 7c shows modelling using the GL calculations expressions for the micro-bridge current-phase relationship, with symmetric inductances of 0.7pH in each arm, and a best fit value of $\lambda_{eff}(0) = 173$ nm. This is to be compared with $\lambda_L(0) = 44$ nm for bulk Nb with a T_c of 9.26K [18]. As can be seen from Figures 7c and 8, the full modelling predicts the temperature dependence of the SQUID critical current well, shows a triangular $I_c(\Phi)$ dependence, and does significantly better than that using a sinusoidal current-phase relationship for the modulation depth.

DISCUSSION

Our data shows that the modulation depth is reduced compared to the short bridge model as soon as the coherence length becomes shorter than the bridge length. This effect is much more pronounced in the case of Nb as the intrinsic short coherence length of Nb leads rapidly to values of S/ξ larger than 1. The model describes very well the overall lineshape in the case of both the Al micro-

SQUIDS, as well as the Nb micro-SQUIDS, which show pronounced triangular $I_c(\Phi)$ characteristics. It is remarkable that the Nb micro-SQUIDS show quantum interference at all temperatures, even when the micro-bridges are much longer than the coherence length, and the phase gradients and supercurrent density depressions extend throughout the body of the SQUID. This implies that the heat dissipation that takes place when the SQUID enters the voltage state occurs well outside of the micro-bridge regions.

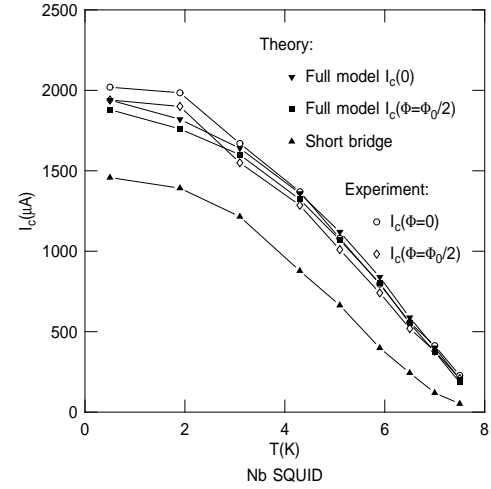


FIG. 8. Plot of the experimentally measured critical currents at zero field (open circles) and at an applied flux of half the full modulation period (open diamonds), for a Nb micro-SQUID, as a function of temperature. The solid triangles are modelling as described in the text for the conventional sinusoidal current-phase relationship. The solid inverted triangles and squares are modelling using the full Ginzburg-Landau calculations for the current-phase relationship, as described in the text.

How can the sensitivity of these micro-SQUIDS be improved? The Nb SQUIDS are limited in their sensitivity by the short coherence length of Nb, as the modulation depth is maximal if the coherence length is equal to or longer than the bridge length. The coherence length could be increased by increasing the mean free path (epitaxial films or thicker layers), but an increase in critical current must be avoided. The performance of these micro-SQUIDS could be improved by significantly reducing the length of the Dayem bridges, perhaps using novel scanning probe techniques [19]. Decreasing thickness and width of the micro-bridge may lead to a diminution of the mean free path and thus to a diminution of the coherence length. A further way to increase sensitivity of Al as well as Nb micro-SQUIDS may be the suppression of thermal hysteresis. A non-hysteretic behavior may be attained by fabricating the entire SQUID on a normal metal plane in order to remove the heat produced by the non local phase relaxation in the microSQUID. The non-hysteretic behavior will enhance the intrinsic bandwidth

and allow for a standard DC-SQUID detection scheme.

CONCLUSION

In summary, the temperature and field dependence of the critical currents in micro-SQUIDs can be understood by means of numerical calculations based on the phase dependence of the critical current predicted by a 2-d Ginzburg-Landau numerical calculation. It is important to do this calculation for the full micro-SQUID structure in many cases, because of the spreading of the variation in the superconducting phase and depression in the supercurrent density beyond the micro-bridge region in this type of device.

ACKNOWLEDGMENTS:

J. K. would like to thank F. Tafuri for useful conversations, and the Université Joseph Fourier of Grenoble for their support during his visit in 1998, and A. Benoit is thanked for his encouragement of this work.

-
- [1] C. Chapelier, M. El Khatib, P. Perrier, A. Benoit and D. Mailly SQUID 91, Superconducting devices and Their Applications, edited by H. Koch and H. Lübbig (Springer-Verlag, Berlin, 1991) 286-291.
 - [2] C. Chapelier, A. Benoit and D. Mailly, *Phys. Rev. Lett.*, **70** (1993) 2020.
 - [3] W. Wernsdorfer, E. Bonet Orozco, K. Hasselbach, A. Benoit, B. Barbara, N. Demoncy, A. Loiseau, H. Pascard and D. Mailly, *Phys. Rev. Lett.*, **70** (1997) 1791.
 - [4] M. Jamet, W. Wernsdorfer, C. Thirion, D. Mailly, V. Dupuis, P. Mélinon, and A. Pérez, *Phys. Rev. Lett.* **86** (2001) 4676.
 - [5] K. Hasselbach, C. Veauvy, D. Mailly, *Physica C* **332** (2000) 140.
 - [6] C. Veauvy, K. Hasselbach, and D. Mailly, *cond-mat/0110196*.
 - [7] T.A. Fulton, L. NN. Dunkleberger and R.C. Dynes, *Phys. Rev. B.* **6**, 855 (1972).
 - [8] K.K. Likharev and L.A. Yakobson, *Sov. Phys. Tech. Phys.*, **20**, 950 (1976) (*Zh. Tekh. Fiz.* **45**, 1503-1509 (1975)).
 - [9] K.K. Likharev, *Rev. Mod. Phys.* **51**, 101 (1979).
 - [10] E.P. Harris and R.B. Laibowitz, *IEEE Trans. Magn.* **MAG-13**, 724 (1977).
 - [11] W.-T. Tsang and T. Van Duzer, *J. Appl. Phys.* **47** (1976) 2656.
 - [12] M. Faucher, T. Fournier, B. Pannetier, C. Thirion, W. Wernsdorfer, J.C. Villegier, and V. Bouchiat, Proceedings of SQUID 2001, to be published in *Physica C*.
 - [13] M. Tinkham, *Introduction to Superconductivity*, (Mcgraw-Hill, New York, 1975).
 - [14] W.T. Vetterling, S.A. Teukolsky, W.H. Press, and B.P. Flannery, *Numerical Recipes Example Book [C]*, Second Edition, Cambridge, New York, 1988, p. 284.
 - [15] A. Baratoff, J.A. Blackburn, and B.B. Schwartz, *Phys. Rev. Lett.* **25** (1970) 1096.
 - [16] M.D. Maloney, F. de la Cruz, and M. Cardona, *Phys. Rev. Lett.* **5**, 3558 (1972).
 - [17] Jacox and Ketchen, *IEEE Trans. Magn.* **MAG-17** (1981) 400.
 - [18] A. Barone and G. Paternó, *Physics and Applications of the Josephson Effect*, Wiley, New York (1982) p. 200.
 - [19] V. Bouchiat, M. Faucher, C. Thirion, W. Wernsdorfer, T. Fournier, and B. Pannetier, *Appl. Phys. Lett.* **79** (2001) 123.